

Differentiable graph neural network simulator for forward and inverse modeling of multi-layered slope system with multiple material properties

Yongjin Choi^a, Jorge Macedo^a, Chenying Liu^a

^a*School of Civil and Environmental Engineering, Georgia Institute of Technology, Atlanta, 30332, GA, USA*

Abstract

Graph neural network simulators (GNS) have emerged as a computationally efficient tool for simulating granular flows. Previous efforts have been limited to simplified geometries and material characterizations, typically considering only friction angle, which does not reflect the complexity of realistic geotechnical systems such as slopes encountered in engineering practice. This study introduces a differentiable GNS framework designed for multi-layered slope systems comprising both forward and inverse modeling components. The forward component relies on a fine-tuned GNS that incorporates both friction angle and cohesion. Its performance is demonstrated through column collapse and multi-layered slope runout simulations, where GNS replicates multi-material flow dynamics while achieving up to $145\times$ computational speedup over the Material Point Method (MPM). The inverse modeling component leverages the trained GNS, reverse-mode automatic differentiation, and L-BFGS-B optimization to infer material properties from a target runout geometry. Its performance is demonstrated by back-calculating the material strengths that led to failure-induced runout in a dam system composed of multiple materials. Results are obtained within minutes and show good agreement with the target strength values. The framework introduced in this study provides an efficient approach for forward runout assessments and inverse strength back-calculation in realistic slope systems.

Keywords: Inverse analysis, Granular flows, Differentiable simulator, Graph neural networks, Dam failure, Slope runout,

1. Introduction

Granular flow geohazards, such as natural landslides and failures of geotechnical slope systems (e.g., water and tailings dams, heap leach pads, landfills), pose significant risks to infrastructure and human safety, as evidenced by numerous well-documented failures (e.g., the Fundao, Cadia, and Brumadinho dam failures) (Morgenstern et al., 2016; Macedo et al., 2024a; Robertson et al., 2019). Runout assessments are key for understanding the dynamics of granular flows in slope systems and developing effective mitigation strategies. In fact, such assessments are becoming a key component in dam engineering (International Council on Mining & Metals, 2019). Numerical approaches capable of capturing large deformations and the complex mechanics of granular flows have been increasingly used in runout modeling. Examples of recent efforts include the Oso landslide (Yerro et al., 2019), the Cadia dam failure (Macedo et al., 2024b), and the Caloveto landslide (Troncone et al., 2022). However, numerical frameworks face notable computational challenges, particularly in large-scale simulations. For example, particle-based methods like the Discrete Element Method (DEM) (Staron and Hinch, 2005; Kermani et al., 2015; Cleary and Sawley, 2002) simulate micro-structural particle-to-particle interactions but become computationally prohibitive when modeling large-scale flow scenarios that involve a large number of particles and contact interactions. Conventional continuum-based approaches, such as the Finite Element Method (FEM), struggle with large deformations in granular flows due to mesh distortion (Sordo et al., 2024). The Material Point Method (MPM) (Mast et al., 2014; Macedo et al., 2024a; Nguyen et al., 2020a) addresses this limitation by adopting a hybrid Eulerian-Lagrangian approach, but its reliance on repeated mapping between material points and a background grid introduces significant computational overhead. This overhead becomes particularly pronounced in inverse modeling scenarios, which require multiple forward simulations to infer unknown system parameters (Choi and Kumar, 2024b).

Recent advancements in learned physics simulators (Battaglia et al., 2016, 2018; Sanchez-Gonzalez et al., 2020) offer promising alternatives to numerical approaches. Among them, Graph Neural Network Simulators (GNS) (Sanchez-Gonzalez et al., 2020) have emerged as efficient surrogate models for computationally intensive approaches such as DEM (Jiang et al., 2024; Zhao

et al., 2025), MPM (Choi and Kumar, 2024a; Haeri et al., 2024; Kumar and Choi, 2023a; Zhao et al., 2025), and Smoothed Particle Hydrodynamics (SPH) (Li and Farimani, 2022). GNS represents particles as nodes and their interactions as edges in a graph, enabling the model to learn the underlying physics of granular flow dynamics. This structure supports forward predictions with generalization beyond the training domain, similar to numerical frameworks, while achieving computational speedups of several orders of magnitude compared to advanced numerical techniques (Zhao et al., 2025; Choi and Kumar, 2024a). GNS has also shown potential in inverse modeling due to its computational efficiency and inherent differentiability (Zhao et al., 2022; Jiang et al., 2024; Allen et al., 2022). These properties enable rapid exploration of parameter spaces via repeated forward simulations, which would otherwise be prohibitively expensive. Additionally, differentiability allows for gradient-based optimization in high-dimensional inverse problems (Allen et al., 2022; Jiang et al., 2024; Choi and Kumar, 2024b; Kumar and Choi, 2023b). Despite the discussed GNS potential, prior GNS-based efforts relevant to slope systems and runout modeling have focused on simplified geometries, often limited to homogeneous slopes and single-parameter material models based solely on friction angle. These simplifications hinder the applicability of GNS to slope systems encountered in engineering practice, which typically involve multi-layered geometries and materials characterized by both friction angle and cohesion, as described by the Mohr-Coulomb failure criterion.

In this study, we present a differentiable GNS framework for forward and inverse modeling of realistic, multi-layered slope systems characterized by friction angle (ϕ) and cohesion (c). We fine-tune a GNS originally trained on frictional materials to incorporate both ϕ and c , enabling it to simulate frictional and cohesive runout behaviors. We evaluate the framework’s forward modeling performance through column collapse and multi-layered slope runout simulations, benchmarking its predictions against MPM results. For inverse modeling, we integrate the trained GNS with reverse-mode automatic differentiation and the L-BFGS-B (Limited-memory Broyden–Fletcher–Goldfarb–Shanno with Box constraints) optimization algorithm to infer material properties from a target runout geometry. This constrained optimization formulation allows the incorporation of prior knowledge, enabling efficient strength back-calculation from post-failure

observations. The proposed framework provides a computationally efficient, physics-consistent approach for both forward runout prediction and inverse strength estimation in realistic slope systems.

2. GNS Framework for Forward and Inverse Modeling

2.1. GNS forward modeling

GNS represents the physical state of a granular flow as a graph, $G = (V, E)$ (Figure 1). The set of vertices $V = \{v_1, v_2, \dots, v_i\}$ corresponds to soil particles or discretized material regions, while the set of edges $E = \{e_{1,1}, e_{1,2}, \dots, e_{i,j}\}$ encodes interactions between them. In our implementation, which uses MPM to generate training data, vertices represent material points, and edges represent their physical interactions.

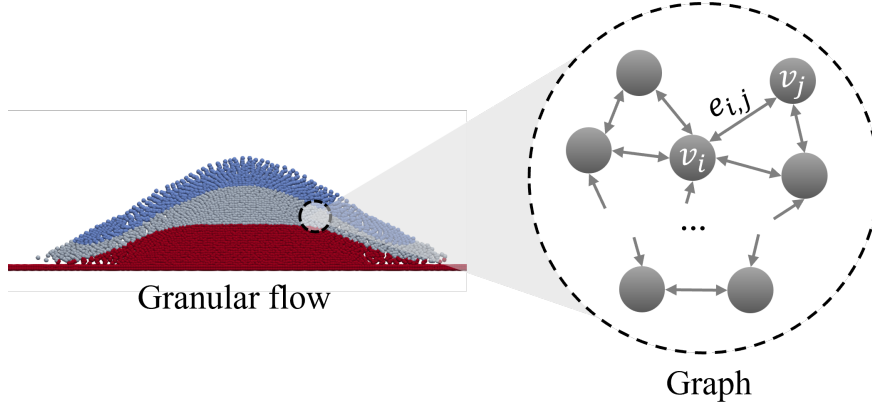


Figure 1: GNS representation of a granular flow. The graph $G = (V, E)$ consists of a set of vertices $V = \{v_1, v_2, \dots, v_i\}$, and edges $E = \{e_{1,1}, e_{1,2}, \dots, e_{i,j}\}$ connecting the vertices.

GNS predicts the physical state of the system at the next timestep $X_{t+1} = \{\mathbf{x}_1^{t+1}, \mathbf{x}_2^{t+1}, \dots, \mathbf{x}_i^{t+1}\}$, given the current state $X_t = \{\mathbf{x}_1^t, \mathbf{x}_2^t, \dots, \mathbf{x}_i^t\}$ as defined in Equation 1.

$$X_{t+1} = GNS(X_t) \quad (1)$$

Each particle's feature vector \mathbf{x}_i^t is defined by Equation 2:

$$\mathbf{x}_i^t = [\mathbf{p}_i^{t-k:t}, \mathbf{b}_i^t, \mathbf{f}, \mathbf{w}] \quad (2)$$

Here, t represents timestep, i denotes the particle index, $\mathbf{p}_i^{t-k:t}$ contains particle positions from $t - k$ to t (we set $k=6$, following Choi and Kumar (2024a)), \mathbf{b}_i^t encodes boundary information, \mathbf{f} denotes the particle type (e.g., stationary or kinematic), and \mathbf{w} encodes material properties. For Mohr-Coulomb materials, $\mathbf{w} = [\phi, c]$. GNS follows an autoregressive rollout scheme, recursively using its own predictions as input to simulate the k th timestep of interest: $X_0 \rightarrow \mathbf{GNS} \rightarrow X_1 \rightarrow \mathbf{GNS} \rightarrow \dots \rightarrow X_{k-1} \rightarrow \mathbf{GNS} \rightarrow X_k$.

GNS comprises two main components: a dynamics approximator \mathcal{D}_Θ (Equation 3) and an update function \mathcal{U} (Equation 4) to perform the computations in Equation 1.

$$Y_t = \mathcal{D}_\Theta(X_t) \quad (3)$$

$$X_{t+1} = \mathcal{U}(X_t, Y_t) \quad (4)$$

The dynamics approximator \mathcal{D}_Θ , parameterized by learnable weights Θ , follows an encoder, processor, and decoder architecture. The encoder maps particle states, X_t , to a latent graph $G = (V, E)$. The encoder consists of the vertex encoder ε^v (Equation (5)) and the edge encoder ε^e (Equation (6)).

$$\mathbf{v}_i = \varepsilon^v(\mathbf{x}_i^t) \quad (5)$$

$$\mathbf{e}_{i,j} = \varepsilon^e(\mathbf{r}_{i,j}^t) \quad (6)$$

where, $\mathbf{r}_{i,j}^t = \left[\left(\mathbf{p}_i^t - \mathbf{p}_j^t \right), \left\| \mathbf{p}_i^t - \mathbf{p}_j^t \right\| \right]$, captures relative displacement and distance of particles at the current timestep.

The processor applies M rounds of message passing to propagate information at the graph vertices along the edges of M -hop neighbors, returning an updated graph $G' = (V', E')$. This step models energy or momentum transfer between particles. Each step $m = 1, 2, \dots, M$ consists of the following operations.

1. **Message construction:** each edge (i, j) produces a message $\mathbf{e}_{i,j}^{(m)}$ using:

$$\mathbf{e}_{i,j}^{(m)} = \phi^e \left(\mathbf{v}_i^{(m-1)}, \mathbf{v}_j^{(m-1)}, \mathbf{e}_{i,j}^{(m-1)} \right)$$

where ϕ^e is a learnable message function.

2. **Message aggregation:** each vertex i collects messages from its neighborhood:

$$\bar{\mathbf{e}}_i^{(m)} = \sum_{j \in \mathcal{N}(i)} \mathbf{e}_{i,j}^{(m)}$$

where $\mathcal{N}(i)$ represents the set of vertices connected to the vertex i .

3. **Vertex update:** each vertex i incorporates the aggregated messages and updates its latent feature:

$$\mathbf{v}_i^{(m)} = \phi^v \left(\mathbf{v}_i^{(m-1)}, \bar{\mathbf{e}}_i^{(m)} \right)$$

where ϕ^v is a learnable vertex update function.

After M iterations of message passing, the processor outputs the updated graph $G' = (V', E')$ with $V' = \{\mathbf{v}_i^{(M)}\}$ and $E' = \{\mathbf{e}_{i,j}^{(M)}\}$. Then, the decoder ($Y_t = \text{Decoder}(G')$) extracts the dynamics $Y_t = \{\mathbf{y}_1^t, \mathbf{y}_2^t, \dots, \mathbf{y}_i^t\}$ for each particle using the decoder function δ (Equation (7)):

$$\mathbf{y}_i^t = \delta \left(\mathbf{v}_i^{(M)} \right) \quad (7)$$

The update function \mathcal{U} uses Y_t to advance the system state to X_{t+1} . \mathcal{U} operates similarly to explicit Euler integration in numerical solvers.

We implement all GNS components—the encoders $\varepsilon^v, \varepsilon^e$, processor functions $\phi^e \phi^v$, and decoder δ —using multilayer perceptrons (MLPs) with two hidden layers of 128 units each. Together, these form the learnable parameter set Θ . We train Θ by minimizing the mean squared error between the predicted accelerations Y_t and ground truth accelerations (i.e., MPM-based) $A_t = \{\mathbf{a}_1^t, \mathbf{a}_2^t, \dots, \mathbf{a}_i^t\}$, using training data generated with MPM simulations based on the CB-Geo codebase (Kumar et al., 2019).

2.2. GNS inverse modeling

Figure 2 illustrates the differentiable GNS framework for back-calculating the strength of selected slope units based on observed runout geometries. The process begins by defining initial conditions and a parameter set, $\boldsymbol{\theta}$, which are input into the GNS for forward simulations. We then compare the simulation results with ground truth data using a loss function $\mathcal{L}_{\boldsymbol{\theta}}$, defined as:

$$\mathcal{L}_{\boldsymbol{\theta}} = \frac{1}{|\mathcal{T}|} \sum_{t \in \mathcal{T}} \left(P_{\boldsymbol{\theta}}^t - \hat{P}_{\boldsymbol{\theta}}^t \right)^2 \quad (8)$$

where $\boldsymbol{\theta}$ denotes the set of model parameters, $P_{\boldsymbol{\theta}}^t$ the observed particle positions at time t , and $\hat{P}_{\boldsymbol{\theta}}^t$ the corresponding simulated positions. The term $|\mathcal{T}|$ represents the number of timesteps included in the loss function. Typically, we evaluate the loss at the final timestep (i.e., $|\mathcal{T}| = 1$)—when the slope system reaches equilibrium—as this is the most commonly available observation for engineering applications. However, we may include multiple timesteps ($|\mathcal{T}| > 1$) if available.

We update material parameters using gradient-based optimization, guided by the gradient of the loss function with respect to $\boldsymbol{\theta}$. The parameter update at iteration i follows:

$$\boldsymbol{\theta}_{i+1} = \boldsymbol{\theta}_i - \eta_i \cdot \mathbf{d}_i \quad (9)$$

Here, η_i is the learning rate, and \mathbf{d}_i is the update direction. First-order methods such as Stochastic Gradient Descent (SGD) or Adaptive Moment Estimation (ADAM) (Kingma, 2014) compute \mathbf{d}_i based on the gradient $\nabla f(\boldsymbol{\theta}_i)$. Second-order methods, such as Broyden–Fletcher–Goldfarb–Shanno (BFGS), improve convergence by incorporating curvature information from the approximate Hessian $H = \nabla^2 f(\boldsymbol{\theta}_i)$, using a history of gradients.

The differentiable GNS framework uses reverse-mode automatic differentiation (AD) (Baydin et al., 2018), which enables efficient and accurate gradient computation. Reverse-mode AD operates in two phases: a forward pass computes and stores intermediate values, and a reverse pass propagates gradients backward through the computational graph using the chain rule. Unlike finite differences, AD computes gradients for all input parameters in a single forward pass, making it highly efficient for high-dimensional inverse problems like slope runout simulations. However,

reverse-mode AD imposes high memory demands, especially in GNS applications involving long simulation rollouts. To manage memory consumption, we implement gradient checkpointing (Chen et al., 2016), which selectively stores key intermediate values and recomputes others during back-propagation. In our implementation, we checkpoint each simulation timestep, which increases forward computation time by $2\text{--}3\times$ but substantially reduces memory usage. Despite this overhead, the differentiable GNS remains significantly faster than high-fidelity solvers (Choi and Kumar, 2024b), making it suitable for inverse analysis of runout in slope systems.

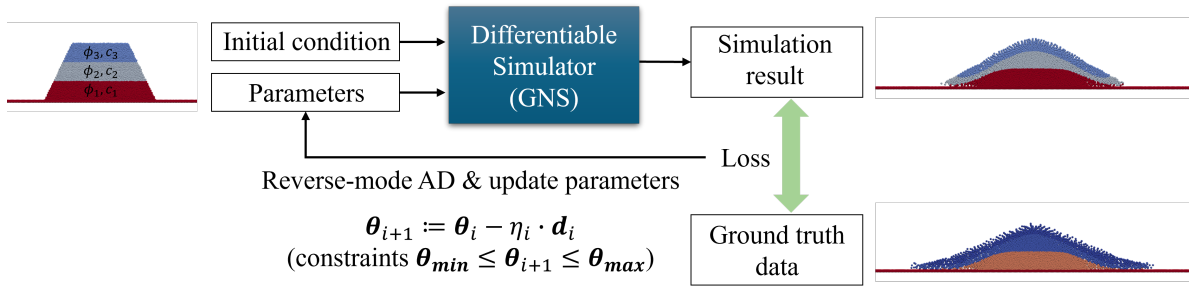


Figure 2: Procedures for solving inverse problems in granular flows with differentiable graph neural network simulator.

2.2.1. Constrained optimization with L-BFGS-B

Back analyses of slope runout failures typically focus on estimating the strength parameters of critical layers involved in the failure mechanism while keeping the properties of non-critical layers fixed (e.g., Lower San Fernando and Las Palmas dams)(Olson, 2001; Moss et al., 2019). Constraining the optimization to fix material properties of noncritical layers narrows the search space, enhances solution stability, and prevents non-physical estimates. We employ L-BFGS-B, a quasi-Newton method that balances fast convergence with low memory usage and supports box constraints on individual parameters. These constraints take the form $\theta_{min} \leq \theta \leq \theta_{max}$, where θ_{min} and θ_{max} are the lower and upper bounds for the parameter set θ . The BFGS algorithm approximates the inverse Hessian using historical gradients and parameter updates, avoiding the $O(n^3)$ cost of computing the true Hessian (Nocedal and Wright, 1999). L-BFGS (Liu and Nocedal, 1989) extends BFGS by limiting memory usage, retaining only a small window of past updates to reconstruct matrix-vector products on demand. L-BFGS-B (Byrd et al., 1995) further enhances this framework by enabling box constraints. During each iteration, L-BFGS-B classifies param-

ters as either fixed (at constraint bounds) or free (within bounds) using gradient-based projection. It then updates only the free parameters using the L-BFGS update rule. This structure ensures compliance with bounds while maintaining the convergence speed of second-order optimization. By incorporating bounds for strength properties, L-BFGS-B guides the inverse modeling process toward physically constrained solutions, making it well-suited for geotechnical applications involving heterogeneous slope systems.

3. Training

We use transfer learning (Feng et al., 2019; Chamangard et al., 2022) to reduce the computational cost and data requirements of training a Graph Neural Network Simulator (GNS), which would otherwise demand extensive granular flow datasets and specialized high-memory GPUs (Choi and Kumar, 2024a). Transfer learning enables a model to reuse previously learned representations rather than learning entirely from scratch. This approach is particularly effective when expanding the capabilities of a simulator to take into account additional material parameters or previously unmodeled physical processes.

We implement a two-stage training strategy. In the first stage, we train a base GNS model on a dataset in which material behavior depends solely on the friction angle. This phase establishes a pre-trained model that captures the core dynamics of frictional granular flows. In the second stage, we fine-tune this model using a smaller, targeted dataset that incorporates both friction and cohesion. This sequential training allows the model to integrate cohesion effects while retaining its learned understanding of frictional behavior. The following section describes the base dataset used in the initial training and details the subsequent fine-tuning procedure.

3.0.1. Datasets

Table 1 summarizes the datasets and MPM configurations used for training the base model and fine-tuning stages. While both datasets share consistent MPM settings (element size, number of material points per cell, and timestep), they differ in material properties: the base dataset considers only friction angle, while the fine-tuning dataset includes both friction angle and cohesion. Geostatic stress conditions are applied in all simulations to capture initial slope stress states, and

Table 1: Datasets for training base model and model fine-tuning.

Property		Dataset	
		Base	Fine-tuning
MPM configuration	Boundary (m)	300 x 152	400 x 152
	Element (m)	4 x 4	
	# material points per cell	4	
	Total # material points	6K	
	timesteps	400	
	dt	0.375	
Material	ϕ ($^{\circ}$) ^a	10 to 40	3 to 35
	c (kPa) ^a	None	10 to 60
	E (MPa)	40	
	ρ (kg/m^3)	1800	
	ν	0.3	
# simulations		2000	1000

^a Friction is normalized using $\tan(\phi)$ and cohesion divided by 100 kPa to facilitate convergence during training.

MPM simulations are run. The base dataset contains 2,000 simulations, using four geometric configurations shown in Figure 3a–d. Solid lines define the granular mass boundaries. The fine-tuning stage also considers additional scenarios of column collapse runout (27 simulations) to complement the training. The column widths and heights range between 50 and 100 m.

In Figure 3a, the gray range bars indicate the allowable variation in the height and width of rectangular granular masses. The black arrows represent the initial velocity v_x, v_y applied to the body ranging from -15 m/s to 15 m/s. We randomly place up to three such rectangles per simulation. In Figure 3b–d, the gray range bars show the spatial variation allowed for the vertices defining the slope geometries. Each configuration contributes 500 simulations. Configuration (a) focuses on frictional-collisional flow, while configurations (b–d) represent multi-layered slopes. In contrast, the fine-tuning dataset focuses on multi-layered slope scenarios and omits the configuration in Figure 3a. Of the 1,000 simulations in the fine-tuning dataset, 250 follow the geometry in Figure 3b, 250 in Figure 3c, and 500 in Figure 3d. For this final configuration, we extend the simulation domain width from 300 m (used in the base dataset) to 400 m to better capture longer runout trajectories.

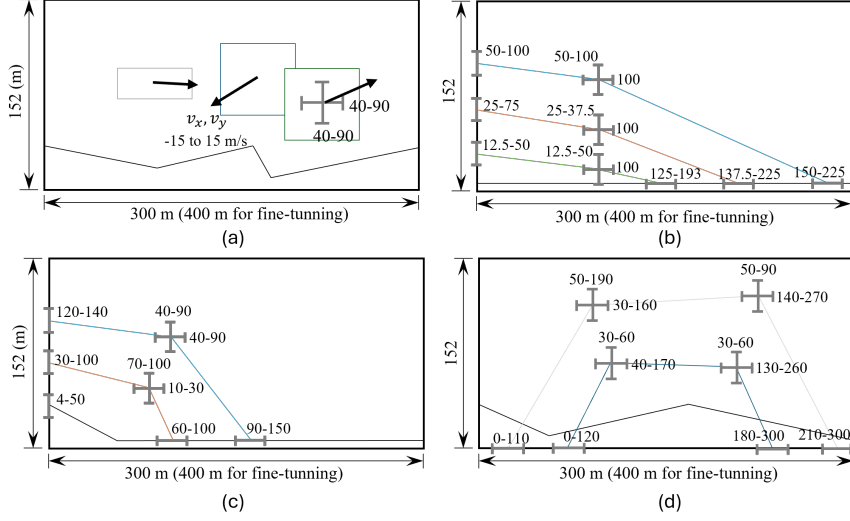


Figure 3: Training data configurations. The figures are not in scale. For the base dataset, all the configurations from (a) to (d) are included. For the fine-tuning dataset, we exclude (a), and additional column collapse scenarios were included. Solid lines define the general shape that outlines the granular mass, with black solid lines representing bedrock. The range bar in subfigure (a) indicates the height and width variation range of the rectangular granular mass to introduce variety to the training data. Similarly, the range bars in Figure 3b-d indicate the allowable spatial variation of vertices connecting the solid lines. The black arrows in subfigure (a) represent the initial velocity v_x, v_y applied to the body.

3.0.2. Model fine-tuning

We train the GNS on the base dataset for 4.1 million steps before initiating fine-tuning. Figure 4 shows the training loss history, computed as the mean squared error (MSE) of one-step acceleration predictions from Equation (3). The figure illustrates two distinct phases: base training (light and dark blue for raw and moving-average losses), where only friction is considered, and fine-tuning (light and dark green), where both friction and cohesion are considered.

During the base training phase, the loss steadily decreases as the model learns to predict the dynamics of frictional granular flows. At the onset of fine-tuning (see the inset plot showing the enlarged part of the transition between the base training phase and the fine-tuning phase), the loss shows a short surge due to the introduction of the previously unseen material property (cohesion) but quickly drops within $\sim 1,000$ steps and stabilizes after an additional $\sim 7,000$ steps. The stabilized loss (~ 0.009 , after around $4.108e6$ steps) is lower than the final loss at the end of base training (~ 0.013 , at around $4.1e6$ steps). This is largely because the fine-tuning dataset excludes high-velocity collision simulations from Figure 3a, which tend to produce higher MSE values (\sim

0.02) and increase the base training loss. Overall, the loss history indicates an adequate transition from base training to fine-tuning, suggesting that the model successfully incorporates cohesive behavior without notable degradation of its prior knowledge about frictional dynamics.

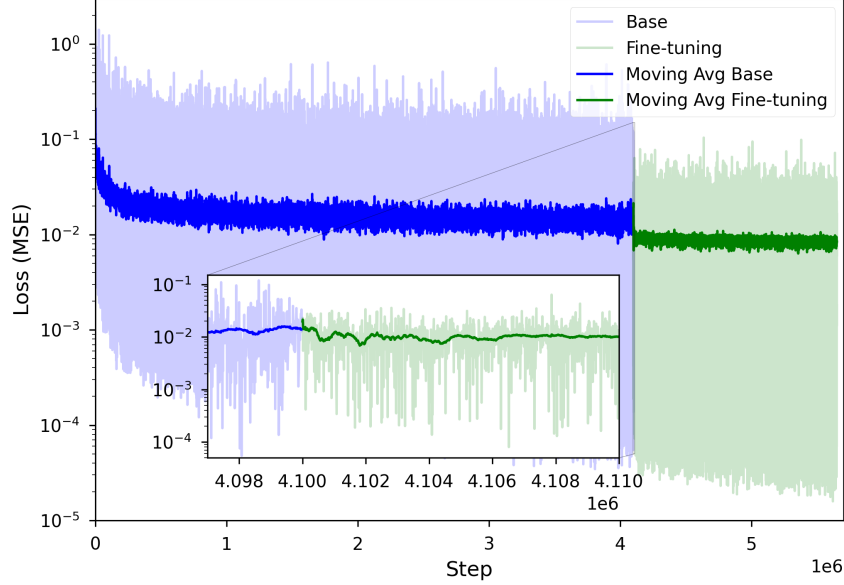


Figure 4: Training loss history. The light blue and dark blue lines represent the raw loss history and its moving average during training on the base dataset. The light green and dark green lines correspond to those during training on the fine-tuning dataset. The inset plot shows the enlarged part of the transition between the base training phase and the fine-tuning phase.

4. Performance Assessment and Applications

4.1. Forward simulation

4.1.1. Granular column collapse with Mohr-Coulomb properties

We evaluate the performance of the fine-tuned GNS model on Mohr-Coulomb-type materials using the granular column collapse experiment—a well-established benchmark for studying granular flow dynamics under controlled conditions (Nguyen et al., 2020b; Lajeunesse et al., 2005). The setup consists of a vertical column of granular material placed on a flat, rigid surface that collapses under gravity.

The runout dynamics are primarily governed by the column’s initial aspect ratio $a = H_0/L_0$, where H_0 and L_0 are the initial height and base length, respectively. At low aspect ratios, only the

column’s edge fails and flows, while the interior remains largely static due to internal friction. At high aspect ratios, most of the column collapses, and the upper portion undergoes near free-fall, resulting in longer runout distances. We quantify runout using the normalized runout distance: $L^n = (L_f - L_0)/L_0$, where L_f is the final runout distance. We assess GNS performance across three aspect ratios: short ($a = 0.5$), intermediate ($a = 1.0$), and tall ($a = 2.0$), corresponding to initial column sizes of 200×100 m, 150×150 m, and 100×200 m, respectively. Each case is simulated using both GNS and MPM. We consider a range of material parameters: friction angles $\phi = (0, 11.25, 22.5, 33.75, 45)^\circ$ and cohesion values $c = (10, 25, 40, 55, 70)$ kPa. Of note, we considered test cases with features that were not included during training. For example, we included different material properties including very low and high friction angles ($\phi = 0, 45^\circ$), high cohesion value ($c = 70$ kPa), longer simulation durations (600 vs. 400 timesteps), and larger granular bodies (e.g., 200 m column height).

Figure 5 shows time evolution examples of granular flows in both GNS and MPM simulations. We compute the error as the absolute percentage difference between the normalized runout predicted by MPM and GNS: $\frac{|L_{MPM}^n - L_{GNS}^n|}{L_{MPM}^n} \times 100$. Figure 5a presents the case with $a = 1.0$, $\phi = 45^\circ$, $c = 10$ kPa) where the GNS predicts a normalized runout of 0.863 compared to 0.848 from MPM, yielding a 1.73% error, ranked at the 25th percentile among all column collapse test cases. Figure 5b shows the case with $a = 1.0$, $\phi = 22.5^\circ$, $c = 70$ kPa, where the normalized runout from GNS and MPM is 1.039 and 1.088, respectively, showing a runout error of 7.64%, ranked at the 50th percentile. Figure 5c shows the case with $a = 2.0$, $\phi = 33.75^\circ$, $c = 10$ kPa, where the normalized runout from GNS and MPM is 2.316 and 2.102, respectively, showing a runout error of 9.27%, ranked at the 75th percentile. In general, GNS captures the overall runout patterns, runout extent, and geometry evolution adequately. Even considering the 75th percentile error case (Figure 5c) where GNS estimates a larger runout, the error is less than 9.27%, and the overall runout patterns are also captured.

Figure 6 presents the comparison between normalized runout distances between MPM and GNS across all considered combinations of cohesion and friction angle. The three subplots correspond to column configurations with different initial aspect ratios: $a = 0.5$ (Figure 6a), $a = 1.0$ (Figure 6b),

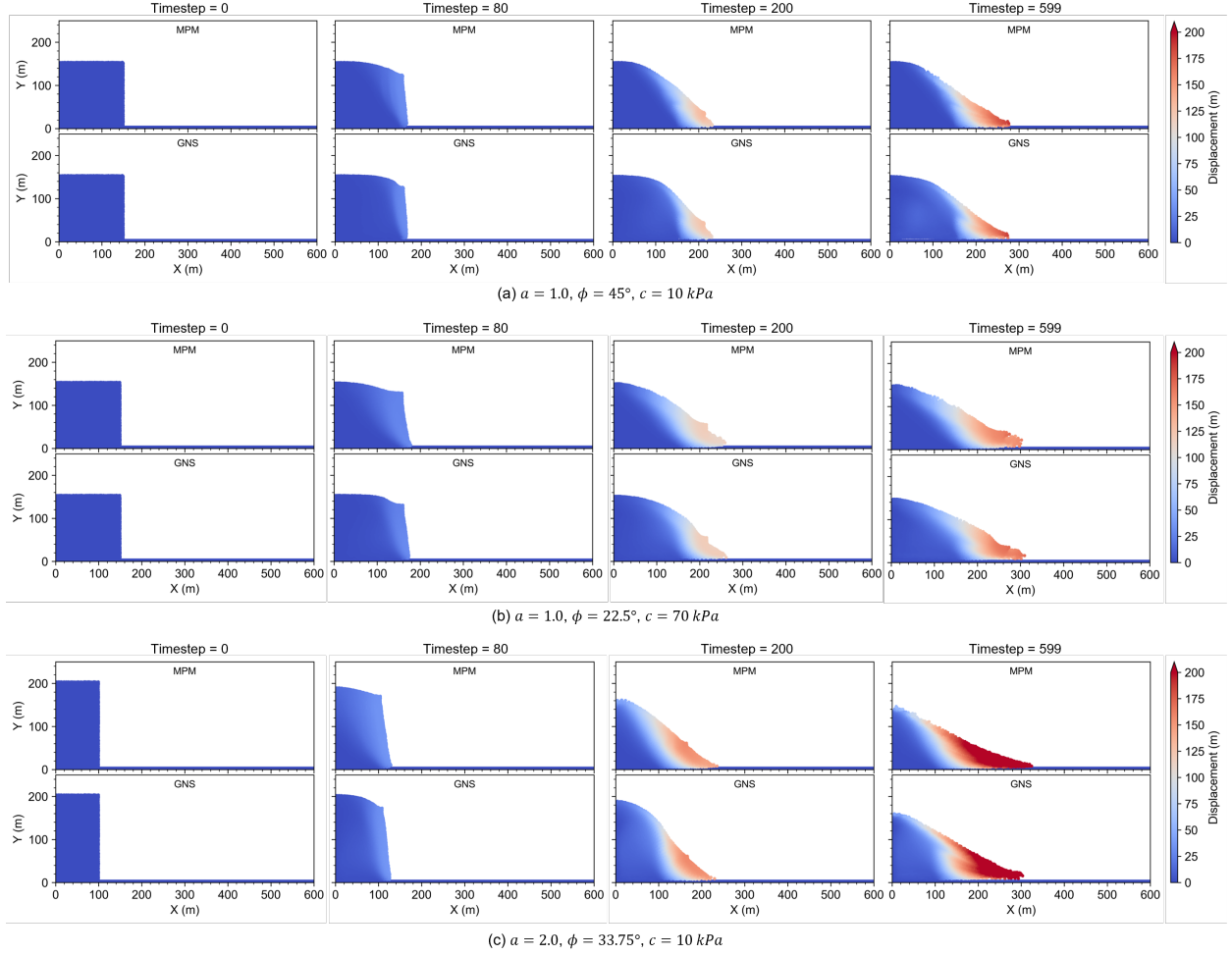


Figure 5: GNS versus MPM granular flow evolution over time. (a) Case with $a = 1.0$, $\phi = 45^\circ$, $c = 10 \text{ kPa}$, showing a runout error of 1.73%, ranked at the 25th percentile among all test cases. (b) Case with $a = 1.0$, $\phi = 22.5^\circ$, $c = 70 \text{ kPa}$, showing a runout error of 7.64%, ranked at the 50th percentile. (c) Case with $a = 2.0$, $\phi = 33.75^\circ$, $c = 10 \text{ kPa}$, showing a runout error of 9.27%, ranked at the 75th percentile.

and $a = 2.0$ (Figure 6c). Each point represents a unique combination of friction angle and cohesion, with color indicating the material configuration as shown in the legend.

The GNS runout predictions show good agreement with MPM results, closely aligning near the 1:1 line in each plot, yielding coefficients of determination (R^2) of 0.975, 0.994, and 0.957 for $a = 0.5$, 1.0, and 2.0, respectively. Figure 6c ($a = 2.0$) shows the largest deviations compared to the other cases, particularly for the material property labels 0 to 6, which have zero or near-zero friction angles or low cohesion values. These configurations exhibit a near free-fall, fluid-like behavior characterized by high accelerations and rapid velocities, amplifying the sensitivity of runout predictions. Moreover, this highly dynamic flow regime deviates significantly from the scenarios used for training. These factors likely contribute to the larger runout errors compared to the other shorter columns.

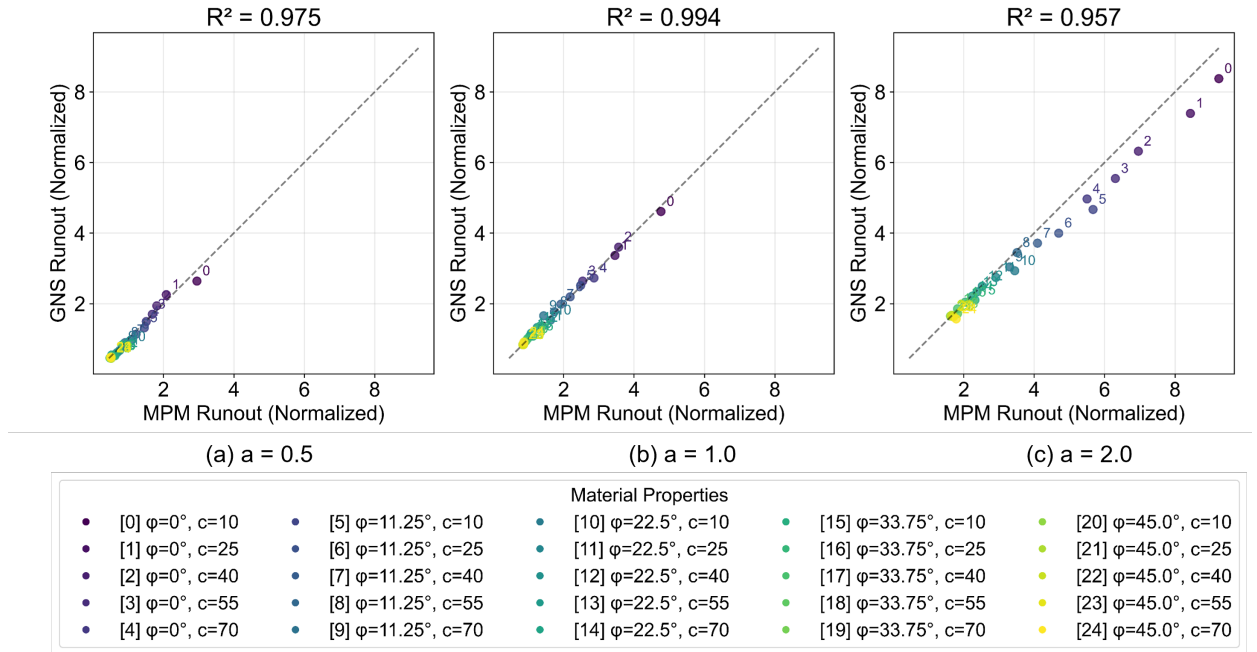


Figure 6: Comparison between normalized runout distances for the granular column collapse test cases between MPM and GNS with different friction angles (ϕ) and cohesions (c).

Figure 7 presents the absolute percentage runout errors across all test cases shown in Figure 6, categorized by column aspect ratio. The mean runout errors for $a = 0.5$, $a = 1.0$, and $a = 2.0$ are 7.26%, 3.55%, and 6.73%, respectively. Among the three, the $a = 1.0$ case (Figure 7b) exhibits the lowest overall errors. However, the highest error is observed at $\phi = 11.25^\circ$ and $c = 70$ kPa,

a cohesion value not included in the training data. For $a = 2.0$ (Figure 7c), higher errors appear in the low friction and cohesion cases, as already discussed in Figure 6. For $a = 0.5$ (Figure 7b), moderately elevated errors appear in some low cohesion cases ($c = 10$ – 25 kPa), but no distinctive trends exist. The model generalizes well to untrained material properties, such as $\phi = 45^\circ$ and $c = 70$ kPa, except for a few outliers (e.g., $a = 1.0$, $\phi = 11.25^\circ$, $c = 70$ kPa). Although the fine-tuning dataset excludes friction angles above $\phi = 35$, the model likely benefited from prior exposure to high-friction scenarios during base training. This result suggests that fine-tuned GNS retains previously learned representations. Overall, the model maintains reliable accuracy within the trained ranges of ϕ and c , while demonstrating reasonable extrapolation performance in untrained regions. Most test cases result in smaller errors than the visual example shown in Figure 5c, which still captures the overall runout profile.

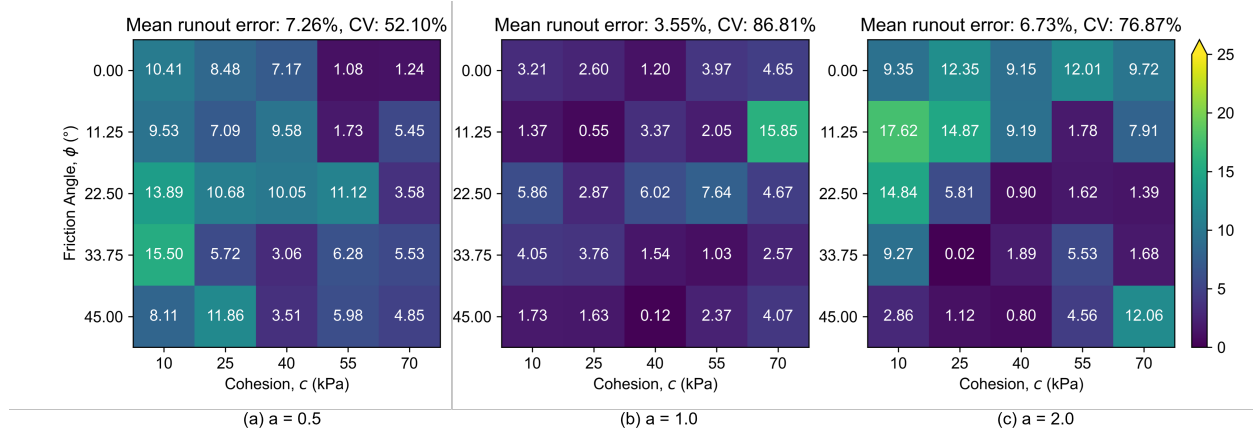


Figure 7: Heatmaps of absolute runout error (%) between GNS and MPM across different combinations of friction angle (ϕ) and cohesion (c) for three column aspect ratios: $a = 0.5$ (left), $a = 1.0$ (middle), and $a = 2.0$ (right). The mean and coefficient of variation (CV) are shown in the subfigure title.

4.1.2. Multi-layered slope runout

We evaluate the GNS model performance on the multi-layered slope system presented in Figure 8 (timestep 0 shows the initial configuration). The system consists of four layers with different material properties. The width of the slope is 300 m, and the height is 150 m. The simulation domain spans 1000 m horizontally and 200 m vertically, exceeding the training domain dimensions (300×152 m or 400×152 m). Additionally, the slope's four interacting layers also surpass the

three-layer limit of the training configurations (refer to Table 1 and Figure 3).

The first layer (material 1, top layer) has a friction angle $\phi = 35^\circ$ and cohesion $c = 4 \text{ kPa}$. The second layer (material 2, the layer below the first layer) has a friction angle $\phi = 15^\circ$ and cohesion $c = 30 \text{ kPa}$. The third layer (material 3, the layer below the second layer) has a friction angle $\phi = 20^\circ$ and cohesion $c = 20 \text{ kPa}$. The fourth layer (material 4, the bottom layer) has a friction angle $\phi = 30^\circ$ and cohesion $c = 10 \text{ kPa}$. The subsequent subfigures (Figure 8) show the failure evolution with time at key timesteps 0, 80, 180, and 479.

We first examine the evolution of the material distribution and runout patterns Figure 8. At timestep=80, the system shows the onset of large movements. The edges of the layers start to displace outward while maintaining their layered structure. The inner parts experience minimal movement. These deformation patterns appear nearly identical between MPM and GNS.

By timestep=180, the flow progresses further, with significant spreading and deformation observed in both simulators. The layered structure is preserved in both MPM and GNS, and the materials continue to displace outward, with the edges of each layer leading the deformation. Both simulations predict similar geometries, with the materials maintaining their relative positions and layering.

At the final timestep, the flow reaches equilibrium. Both simulators exhibit a similar flow profile with the layered structure preserved. The materials show a stretched and flattened bell-shaped geometry, with the third layer (Material 3, red-colored) undergoing the greatest lateral displacement, while the bottom material (Material 4, pink-colored) experiences less movement, entrapped by the other upper layers. Only the flanks of the bottom layer deform, with the inner central part experiencing less displacement. This deformation pattern is captured by the GNS simulations. The intermediate layers (materials 2 and 3) form the thin tail layers between the top and bottom layers along both ends of the deposit. GNS successfully captures this subtle layer formation with a thickness similar to that of MPM. The results presented in this section highlight the GNS's ability to simulate multi-layered material interactions. The runout error estimated based on $x = 500 \text{ m}$ (symmetric x location) is 1.57% on the left side of the flow and 0.96% on the right side of the flow, again highlighting the adequate GNS's performance.

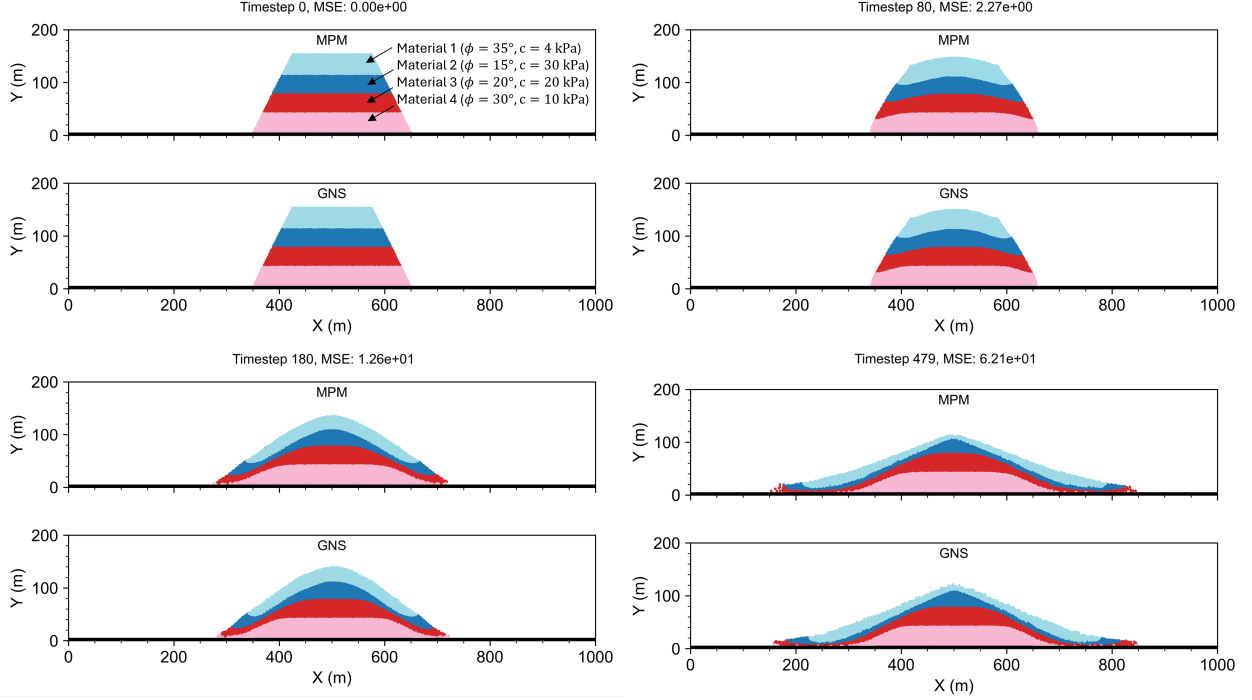


Figure 8: Flow evolution in a layered slope system simulated using MPM and GNS. The slope consists of four materials with varying properties, labeled with different colors. The evolution is illustrated at four timesteps: 0, 80, 180, and 479. The material property values are shown in the figure at the timestep 0.

Figure 9 shows the displacement field evolution associated with Figure 8. At timestep=80, GNS captures the collapse development well. The highest displacement is concentrated along the outermost edges, shown in light blue, while the central region remains stationary in dark blue. GNS successfully tracks the intermediate progress of the flow (see timestep=180), with the highest displacement continuing to occur at the slope's flanks. At timestep 479, the last timestep when the flow reaches equilibrium, the displacement field of GNS closely aligns with MPM, with a clear concentration of displacement on the left and right slopes. Finally, we also assess the computational efficiency of GNS relative to MPM for the configuration shown in Figure 8. MPM simulations were performed on the Frontera supercomputer at the Texas Advanced Computing Center (TACC) using an Intel Cascade Lake processor with 56 cores, while GNS simulations were executed on an NVIDIA Quadro RTX 5000 GPU with 16 GB of memory. The GNS completed the simulation in just 41 seconds, compared to 6,075 seconds for MPM, achieving a speed-up of approximately $145\times$.

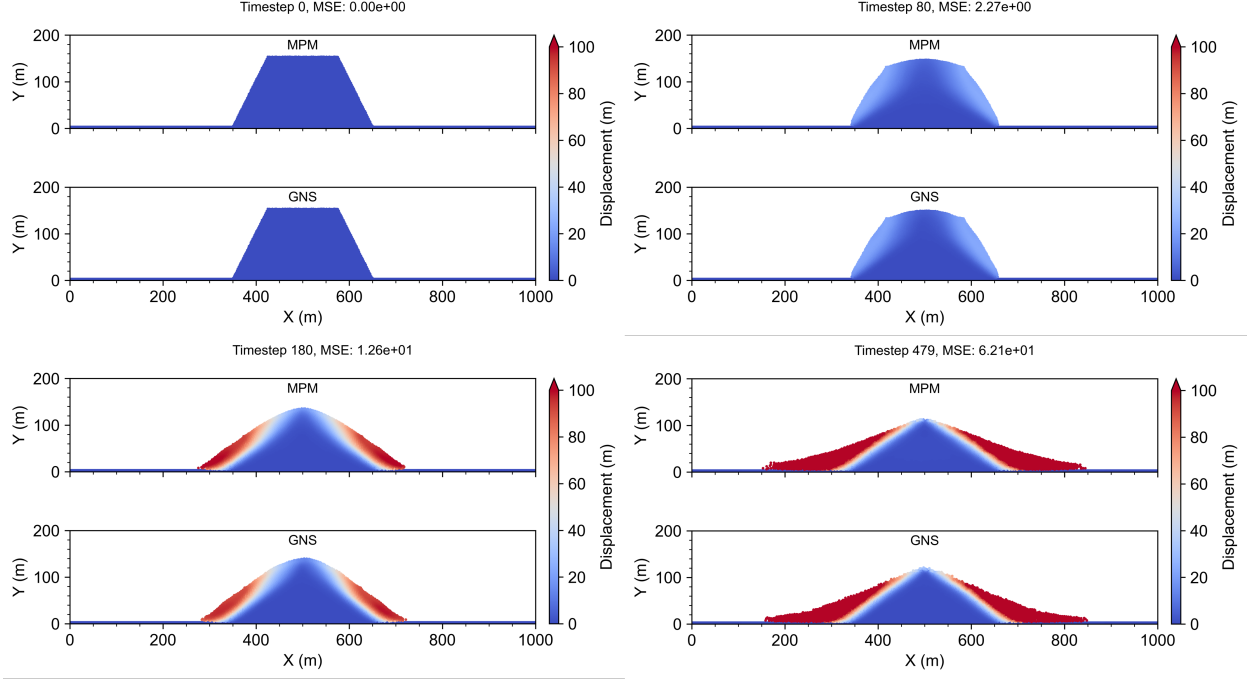


Figure 9: Evolution of granular flow of a dam-shaped multi-layered slope system simulated from MPM and GNS. The color field represents displacement magnitude. The evolution is illustrated at four timesteps: 0, 80, 180, and 479.

4.2. Inverse analysis

This section demonstrates the application of the differentiable GNS framework (see Figure 2) to perform inverse analyses for dam runout scenarios. We use the trained GNS model developed in this study to back-calculate the undrained shear strength of a target material within a multi-material dam system based on the final runout geometry. The initial configuration for the inverse analysis appears in Figure 10a and is not part of the training dataset.

The dam consists of three vertical zones: (1) the upstream shell (sky blue), (2) the core (red), and (3) the downstream shell, which includes two horizontal layers (pink and blue). Table 2 summarizes the true material properties used to generate the runout via MPM. Material 1, representing part of the downstream shell, has an undrained strength of $s_u = 40 \text{ kPa}$, modeled using Mohr–Coulomb parameters $\phi = 0^\circ$, $c = 40 \text{ kPa}$. This strength corresponds to an undrained strength ratio $s_u/\sigma'_v = 0.13$, based on an average depth of 17 m. Material 2 (core) has $\phi = 10^\circ$, $c = 100 \text{ kPa}$; material 3 has $\phi = 41^\circ$, $c = 10 \text{ kPa}$; and material 4 (upstream shell) has $\phi = 42.5^\circ$, $c = 10 \text{ kPa}$. Notably, several of these values fall outside the GNS training range for friction angle

($\phi = 3^\circ$ to $\phi = 40^\circ$, allowing us to evaluate generalization performance.

Table 2: Material properties of the dam shown in Figure 10 and the constraint ranges for each material used in the inverse analysis.

Materials	ϕ ($^\circ$)			c (kPa)		
	True	Min constraint	Max constraint	True	Min constraint	Max constraint
1	0	0	0	40 ^a	10	100
2	10	9.93	10.04	100	99	101
3	41	40.96	41.04	10	9	11
4	42.5	42.46	42.52	10	9	11

^a For the material 1, we assign $\phi = 0^\circ$ and $c = 40$ kPa as a Mohr-Coulomb material parameter to represent its undrained shear strength $s_u = 40$ kPa. This is derived from the assumed shear strength ratio s_u/σ'_v of 0.13 at the average depth of material 1 (17 m).

We use MPM to generate the target final deposit, shown in Figure 10b–c, which serves as the reference for optimization. The objective is to infer the undrained strength of material 1 by adjusting its cohesion to minimize the mismatch between GNS-predicted and MPM-derived final geometries. We assume the strength properties of materials 2–4 are known and enforce tight bounds on their parameters during optimization (see the min and max constraint values in Table 2). This is consistent with standard back-analyses in engineering practice and post-failure forensic investigations (Olson, 2001).

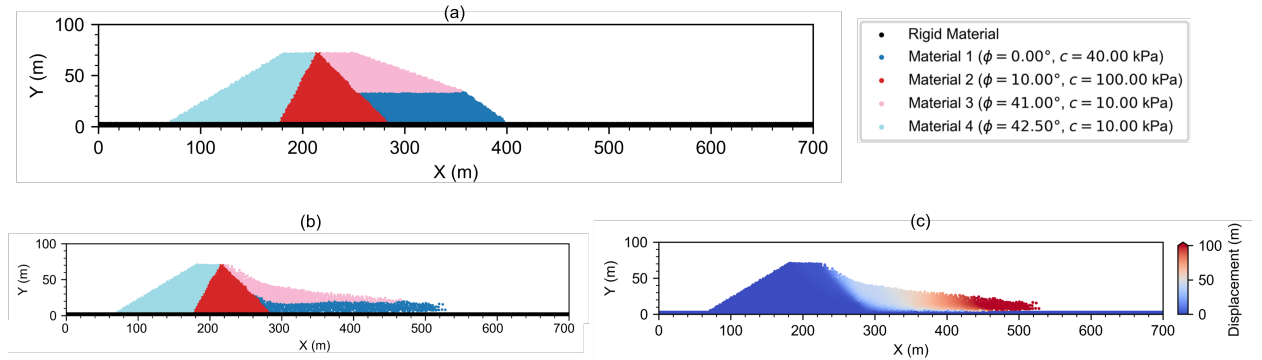


Figure 10: Multi-material dam considered in the inverse analysis. (a) initial configuration, (b) final deposit after failure, (c) displacement field of the final deposit.

We define the inverse loss as the mean squared error (MSE) between GNS-predicted particle positions \hat{P}_θ^t and the target positions P_θ^t from the MPM simulation, using the formulation in Equation (8). Since we only consider the final time step, we set $|\mathcal{T}| = 1$. The optimization process starts by initializing the cohesion of material 1 at $c=90$ kPa.

Figure 11 shows the optimization history. The left panel tracks data loss (MSE between particle positions), and the right panel tracks model loss (MSE between normalized true and inferred parameters). Both metrics decrease steadily, with convergence occurring after approximately seven iterations. Figure 12 shows the change in material parameters during inverse optimization. The cohesion of material 1 (blue dashed line) converges to 46.6 kPa, which is close to the true value of 40 kPa. The estimated strength corresponds to a strength ratio $s_u/\sigma'_v = 0.15$, which is close to the target value of 0.13 . This small discrepancy (~ 0.02) falls within the uncertainty typically encountered in empirical back-analyses (Olson and Stark, 2003). Throughout the optimization, materials 2–4 parameters remain within the imposed bounds, demonstrating that the L-BFGS-B algorithm effectively maintains constraints while achieving convergence.

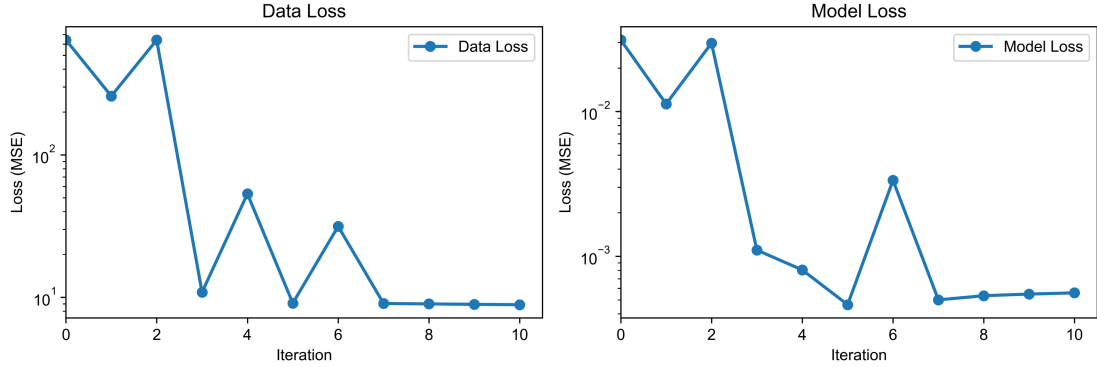


Figure 11: Loss history during optimization. At each iteration, data loss is computed with Equation (8) where the ground truth particle positions P_θ^t is the final deposit obtained from the MPM simulation, and \hat{P}_θ^t is the GNS simulation result with the current material model parameters. The model loss represents the MSE between the normalized true material model properties and the inferred material properties at the current iteration.

Figure 13 illustrates how the estimated runout geometries change during the optimization process. At iteration 0, with $c = 90$ kPa, GNS predicts no deformation. At iteration 1, the optimizer reduces c to 10 kPa, causing excessive runout. As c converges to 46.6 kPa, the GNS-predicted geometry matches the target MPM runout.

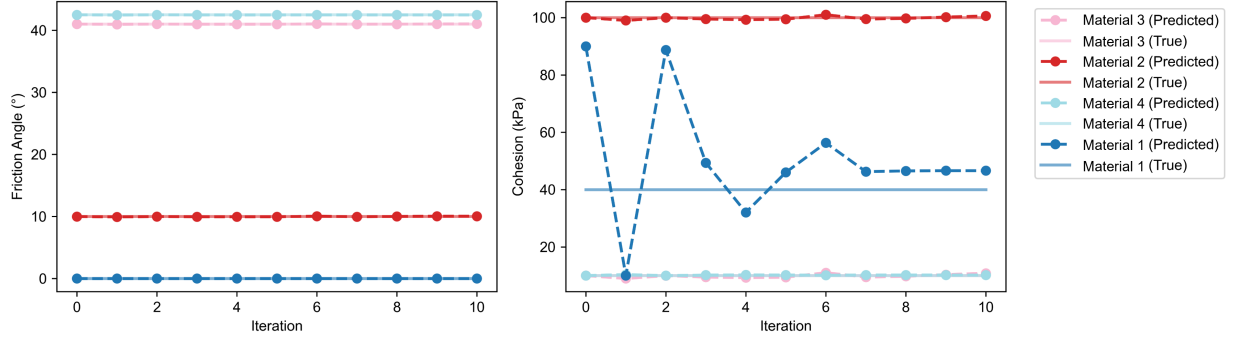


Figure 12: Material model parameter history during the optimization.

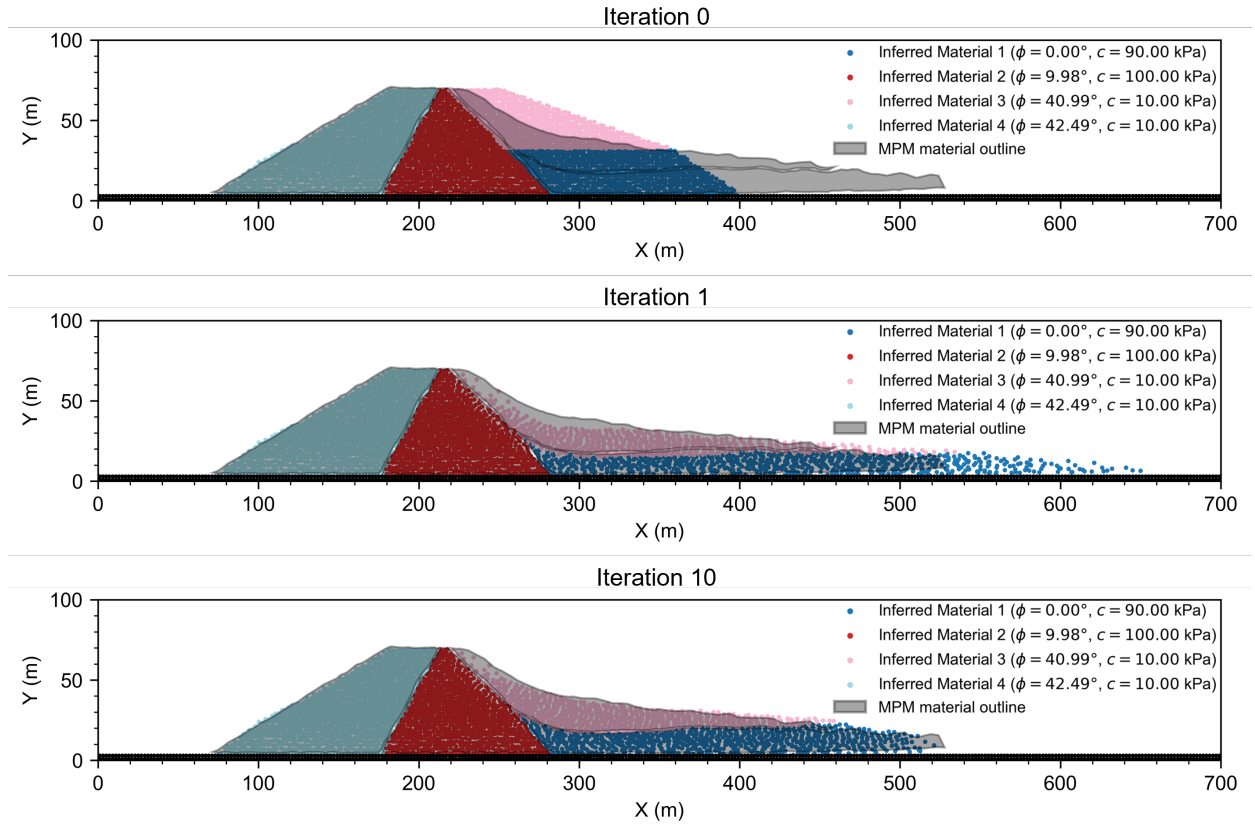


Figure 13: Visualization of GNS prediction during optimization compared to the final deposit from MPM. The legend shows the inferred material properties at each iteration. The black shaded outlines correspond to the final deposit from MPM for each material.

Regarding computational cost, each GNS-based optimization step takes ~ 1 minute on an NVIDIA Quadro RTX 5000, including 20 seconds for forward simulation and 42 seconds for gradient computation. In contrast, a single iteration using a non-differentiable forward model (e.g., MPM) would require over 95 minutes, including 2850 seconds for one MPM run, plus an additional simulation for gradient estimation via finite differences, which are also known for introducing numerical noise. In this context, the computational efficiency of the proposed inversion is remarkable.

5. Conclusion

This study introduces a differentiable Graph Neural Network Simulator (GNS) for forward and inverse modeling of multi-layered slope systems characterized by the Mohr-Coulomb model. We demonstrate that GNS serves as an effective differentiable surrogate model for the Material Point Method (MPM), significantly accelerating both forward and inverse modeling of granular flow simulations in realistic multi-layered slope systems while considering full granular flow kinematics.

Through transfer learning, we fine-tuned a pre-trained GNS model, originally calibrated for a single material property (friction angle), to incorporate cohesion, rather than training a completely new model from scratch. The fine-tuning training loss successfully stabilizes when facing previously unseen granular flow data involving cohesive materials.

For forward modeling, we first evaluate GNS’s performance to simulate Mohr-Coulomb-type materials using granular column collapse experiments. The results show that GNS adequately captures the runout behavior across diverse friction angles and cohesion values. There are larger errors when simulating highly dynamic fluid-like materials outside the training dataset range, but these cases are not common in engineering applications. In general, the errors remain below 10 percent for most scenarios. We then apply GNS to simulate a multi-layered dam runout. GNS accurately reproduces runout dynamics and inter-material interactions, while achieving up to $145\times$ speed-up compared to MPM.

For inverse modeling, we apply the differentiable GNS framework to identify material parameters in a multi-layered slope. By combining GNS-accelerated forward simulation, L-BFGS-B optimization, and reverse-mode automatic differentiation, the proposed approach successfully identified

the undrained shear strength of a selected material in a multi-material dam system within minutes. An equivalent inverse analysis using conventional MPM for forward evaluation and finite differentiation for gradient computation would require several hours of computational time. Although we focus on a single-parameter inversion, because it is the common scenario in back-analyses of slope failures, the proposed framework supports efficient multi-parameter inversion. This is the case because the reverse-mode AD component computes exact gradients for all parameters in a single forward pass, keeping the computational cost nearly constant regardless of parameter count. In contrast, finite difference methods, which would be required with MPM schemes, scale poorly, as they require multiple forward evaluations per parameter.

Lastly, while we considered only the final runout geometry for inversion, the presented GNS framework can accommodate intermediate runout states, enabling more robust optimization. As field instrumentation and remote sensing continue to improve, future case histories are likely to capture the runout progression, making the proposed GNS framework especially well-suited for emerging applications.

This study demonstrates the potential of differentiable GNS as a useful surrogate modeling approach for forward and inverse problems in slope systems, effectively balancing computational efficiency with physical accuracy.

6. Acknowledgment

This study was funded by the TAILENG foundation. Any opinions, findings, conclusions, or recommendations expressed in this study are those of the author(s). We also thank the Texas Advanced Computing Center (TACC) at The University of Texas at Austin for providing Frontera and Lonestar6 HPC resources to support GNS training (<https://www.tacc.utexas.edu>).

References

- Allen, K.R., Lopez-Guevara, T., Stachenfeld, K., Sanchez-Gonzalez, A., Battaglia, P., Hamrick, J., Pfaff, T., 2022. Physical design using differentiable learned simulators. arXiv preprint arXiv:2202.00728 .
- Battaglia, P., Pascanu, R., Lai, M., Jimenez Rezende, D., et al., 2016. Interaction networks for learning about objects, relations and physics. *Advances in neural information processing systems* 29.

- Battaglia, P.W., Hamrick, J.B., Bapst, V., Sanchez-Gonzalez, A., Zambaldi, V., Malinowski, M., Tacchetti, A., Raposo, D., Santoro, A., Faulkner, R., 2018. Relational inductive biases, deep learning, and graph networks. arXiv preprint arXiv:1806.01261 .
- Baydin, A.G., Pearlmutter, B.A., Radul, A.A., Siskind, J.M., 2018. Automatic differentiation in machine learning: a survey. *Journal of Machine Learning Research* 18, 1–43.
- Byrd, R.H., Lu, P., Nocedal, J., Zhu, C., 1995. A limited memory algorithm for bound constrained optimization. *SIAM Journal on scientific computing* 16, 1190–1208.
- Chamangard, M., Ghodrati Amiri, G., Darvishan, E., Rastin, Z., 2022. Transfer learning for cnn-based damage detection in civil structures with insufficient data. *Shock and Vibration* 2022, 3635116.
- Chen, T., Xu, B., Zhang, C., Guestrin, C., 2016. Training deep nets with sublinear memory cost. *CoRR* abs/1604.06174. URL: <http://arxiv.org/abs/1604.06174>, arXiv:1604.06174.
- Choi, Y., Kumar, K., 2024a. Graph neural network-based surrogate model for granular flows. *Computers and Geotechnics* 166, 106015.
- Choi, Y., Kumar, K., 2024b. Inverse analysis of granular flows using differentiable graph neural network simulator. *Computers and Geotechnics* 171, 106374.
- Cleary, P.W., Sawley, M.L., 2002. Dem modelling of industrial granular flows: 3d case studies and the effect of particle shape on hopper discharge. *Applied Mathematical Modelling* 26, 89–111.
- Feng, C., Zhang, H., Wang, S., Li, Y., Wang, H., Yan, F., 2019. Structural damage detection using deep convolutional neural network and transfer learning. *KSCE Journal of Civil Engineering* 23, 4493–4502.
- Haeri, A., Holz, D., Skonieczny, K., 2024. Subspace graph networks for real-time granular flow simulation with applications to machine-terrain interactions. *Engineering Applications of Artificial Intelligence* 135, 108765.
- International Council on Mining & Metals, 2019. Icm, an environment programme and principles for responsible investment agree to co-convene mine tailings storage facilities review. <https://www.icmm.com/en-gb/news/2019/tailings-review>. Accessed: 2019-05-20.
- Jiang, Y., Byrne, E., Glassey, J., Chen, X., 2024. Integrating graph neural network-based surrogate modeling with inverse design for granular flows. *Industrial & Engineering Chemistry Research* .
- Kermani, E., Qiu, T., Li, T., 2015. Simulation of collapse of granular columns using the discrete element method. *International Journal of Geomechanics* 15, 04015004.
- Kingma, D.P., 2014. Adam: A method for stochastic optimization. arXiv preprint arXiv:1412.6980 .
- Kumar, K., Choi, Y., 2023a. Accelerating particle and fluid simulations with differentiable graph networks for solving forward and inverse problems, in: *Proceedings of the SC’23 Workshops of The International Conference on High Performance Computing, Network, Storage, and Analysis*, pp. 60–65.
- Kumar, K., Choi, Y., 2023b. Accelerating particle and fluid simulations with differentiable graph networks for solving forward and inverse problems, in: *Proceedings of the SC ’23 Workshops of The International Conference on High Performance Computing, Network, Storage, and Analysis*, Association for Computing Machinery, New York, NY,

- USA. p. 60–65. URL: <https://doi.org/10.1145/3624062.3626082>, doi:10.1145/3624062.3626082.
- Kumar, K., Salmond, J., Kularathna, S., Wilkes, C., Tjung, E., Biscontin, G., Soga, K., 2019. Scalable and modular material point method for large-scale simulations. arXiv preprint arXiv:1909.13380 .
- Lajeunesse, E., Monnier, J., Homsy, G., 2005. Granular slumping on a horizontal surface. *Physics of fluids* 17.
- Li, Z., Farimani, A.B., 2022. Graph neural network-accelerated lagrangian fluid simulation. *Computers & Graphics* 103, 201–211.
- Liu, D.C., Nocedal, J., 1989. On the limited memory bfgs method for large scale optimization. *Mathematical programming* 45, 503–528.
- Macedo, J., Yerro, A., Cornejo, R., Pierce, I., 2024a. Cadia tsf failure assessment considering triggering and post-triggering mechanisms. *Journal of Geotechnical and Geoenvironmental Engineering* 150, 04024011.
- Macedo, J., Yerro, A., Cornejo, R., Pierce, I., 2024b. Cadia tsf failure assessment considering triggering and post-triggering mechanisms. *Journal of Geotechnical and Geoenvironmental Engineering* 150, 04024011.
- Mast, C.M., Arduino, P., Mackenzie-Helnwein, P., Miller, G.R., 2014. Simulating granular column collapse using the material point method. *Acta Geotechnica* 10, 101–116. doi:10.1007/s11440-014-0309-0.
- Morgenstern, N.R., Vick, S.G., Viotti, C.B., Watts, B.D., 2016. Report on the Immediate Causes of the Failure of the Fundão Dam. Technical Report. Fundão Tailings Dam Review Panel.
- Moss, R., Gebhart, T., Frost, D., Ledezma, C., 2019. Flow-failure case history of the las palmas, chile, tailings dam. PEER Report 1.
- Nguyen, N.H., Bui, H.H., Nguyen, G.D., 2020a. Effects of material properties on the mobility of granular flow. *Granular Matter* 22, 59.
- Nguyen, N.H., Bui, H.H., Nguyen, G.D., 2020b. Effects of material properties on the mobility of granular flow. *Granular Matter* 22, 59.
- Nocedal, J., Wright, S.J., 1999. Numerical optimization. Springer.
- Olson, S.M., 2001. Liquefaction analysis of level and sloping ground using field case histories and penetration resistance. University of Illinois at Urbana-Champaign.
- Olson, S.M., Stark, T.D., 2003. Yield strength ratio and liquefaction analysis of slopes and embankments. *Journal of Geotechnical and Geoenvironmental Engineering* 129, 727–737.
- Robertson, P.K., de Melo, L., Williams, D.J., Wilson, G.W., 2019. Report of the Expert Panel on the Technical Causes of the Failure of Feijão Dam I. Technical Report. Available from <http://www.bitechnicalinvestigation.com/>.
- Sanchez-Gonzalez, A., Godwin, J., Pfaff, T., Ying, R., Leskovec, J., Battaglia, P., 2020. Learning to simulate complex physics with graph networks, in: International conference on machine learning, PMLR. pp. 8459–8468.
- Sordo, B., Rathje, E., Kumar, K., 2024. Sequential hybrid finite element and material point method to simulate slope failures. *Computers and Geotechnics* 173, 106525.
- Staron, L., Hinch, E., 2005. Study of the collapse of granular columns using two-dimensional discrete-grain simulation. *Journal of Fluid Mechanics* 545, 1–27.

- Troncone, A., Pugliese, L., Conte, E., 2022. Analysis of an excavation-induced landslide in stiff clay using the material point method. *Engineering Geology* 296, 106479. URL: <https://www.sciencedirect.com/science/article/pii/S0013795221004907>, doi:<https://doi.org/10.1016/j.enggeo.2021.106479>.
- Yerro, A., Soga, K., Bray, J., 2019. Runout evaluation of oso landslide with the material point method. *Canadian Geotechnical Journal* 56, 1304–1317.
- Zhao, Q., Lindell, D.B., Wetzstein, G., 2022. Learning to solve pde-constrained inverse problems with graph networks. arXiv preprint [arXiv:2206.00711](https://arxiv.org/abs/2206.00711) .
- Zhao, S., Chen, H., Zhao, J., 2025. A physical-information-flow-constrained temporal graph neural network-based simulator for granular materials. *Computer Methods in Applied Mechanics and Engineering* 433, 117536.